frontiers | Frontiers in Forests and Global Change

TYPE Original Research
PUBLISHED 04 January 2023
DOI 10.3389/ffgc.2022.1052299

OPEN ACCESS

EDITED BY
Nikos Koutsias,
University of Patras, Greece

REVIEWED BY
Ioannis Gitas,
Aristotle University of Thessaloniki, Greece
Olga Viedma Sillero,
University of Castilla–La Mancha, Spain
Emmanouil Psomiadis,
Agricultural University of Athens, Greece

*CORRESPONDENCE
Patricia Oliva
patricia.oliva@uah.es

SPECIALTY SECTION
This article was submitted to Fire and Forests, a section of the journal Frontiers in Forests and Global Change

RECEIVED 23 September 2022
ACCEPTED 23 November 2022
PUBLISHED 04 January 2023

CITATION
Oliva P, Mansilla R, Roteta E and Pérez-Martínez W (2023) Suitability of band angle indices for burned area mapping in the Maule Region (Chile). *Front. For. Glob. Change* 5:1052299. doi: 10.3389/ffgc.2022.1052299

Suitability of band angle indices for burned area mapping in the Maule Region (Chile)

Patricia Oliva[1,2]*, Roxana Mansilla[3], Ekhi Roteta[4] and Waldo Pérez-Martínez[2,3]

[1]Universidad de Alcalá, Environmental Remote Sensing Research Group, Department of Geology, Geography and Environment, Alcalá de Henares, Spain, [2]Hémera Centro de Observación de la Tierra, Escuela de Ingeniería Forestal, Facultad de Ciencias, Ingeniería y Tecnología, Universidad Mayor, Santiago, Chile, [3]Magíster en Teledetección, Escuela de Ingeniería Forestal, Facultad de Ciencias, Ingeniería y Tecnología, Universidad Mayor, Santiago, Chile, [4]Department of Geography, Prehistory and Archaeology, University of the Basque Country, Bilbao, Spain

In January 2017, 114 active fires burned throughout Chile at the same time. These fires spread quickly due to high temperatures, fast dry winds, and low vegetation water content. The fire events burned more than 570,000 ha, from which 20% of the area was endangered native forest. Timely and accurate burned area mapping is crucial for the evaluation of damages and management of the affected areas. As Chile is a diverse country with many types of ecosystems and vegetation, the use of novel spectral indices may improve the accuracy of satellite data-based burned area mapping algorithms. In this study, we explored the contribution of band angle indices (BAnI) to burned area mapping. The BAnI are based on trigonometric equations that proved to be sensitive to moisture conditions. Then, we aimed to test their sensitivity to the burned area spectral signature. We used Sentinel-2 data at 20 m resolution to calibrate and implement a random forest (RF) classifier in Google Earth Engine (GEE) computing platform. We ran the RF classifier with and without BAnI to evaluate their potential to identify burned areas and performed two accuracy assessments comparing the results with visually digitized fire perimeters from (1) WorldView 3 (WV3) images, and (2) Sentinel at 10 m resolution. We determined that both BA classifications were more accurate than the perimeters created by the Chilean National Forest Corporation (CONAF), which overestimates the area burnt. The overestimation of CONAF perimeters is produced by considering as burned the inner unburned areas and omitting some small, burned areas. The first assessment showed no significant differences between the two RF classifications. However, the second validation showed lower omission and commission errors for the RF classifier with the BAnI (5 and 17.8%, respectively). On the other hand, comparing both BA classifications with and without BAnI, we observed differences in the spatial distribution of the errors. However, the RF classification with BAnI offered fewer commission errors located in agricultural areas. The burned area algorithms developed in GEE

showed their potential to map the fire-affected area quickly, efficiently, and accurately, accounting for all the areas burned in the season, including the small and agricultural fires the official perimeters did not consider.

KEYWORDS

random forest, Google Earth Engine, machine learning, satellite images, forest fires

Introduction

Forest fires can be produced naturally by electrical storms or derived from human activity in the territory. Forest fires produce enormous damage to ecosystems and human health, great economic losses, and contribute to climate change through gas emissions and changes in the albedo (van der Werf et al., 2017; Bowman et al., 2020; Johnston et al., 2021). In recent years, fire occurrence and intensity have increased worldwide due to causes derived from global warming, mainly related to prolonged periods of drought and high temperatures (Bowman et al., 2019; Turco et al., 2019). The Australian 2019–2020, the Siberian 2020, and the Canadian 2021 fire seasons are clear examples of the effect of global warming. In addition, the temporal cycles of fire occurrence are often influence by human activity (Benali et al., 2017), as in most biomes fire is mainly caused by humans (Chuvieco et al., 2021).

The detection of burned areas through satellite images has been developed for more than 30 years and is currently considered a fundamental source of information for monitoring systems and contributes to the fulfillment of Sustainable Development Objectives (Chuvieco et al., 2019). Numerous algorithms and methodologies have been developed and applied for burned area detection using all types of sensors, both on a global, regional, and local scale (Dragozi et al., 2014; Boschetti et al., 2015; Chuvieco et al., 2018; Garcia-Lazaro et al., 2018; Giglio et al., 2018; Lasaponara and Tucci, 2019; Lizundia-Loiola et al., 2020). Several studies have shown that operationally produced and publicly available burned area products on a global scale do not meet the needs for rapid access to information or provide the spatial resolution required for strategic post-fire planning at the local level (Tsela et al., 2014; Chuvieco et al., 2019; Valencia et al., 2020; Ramo et al., 2021). Medium spatial resolution satellites, such as Landsat-8 and the Sentinel-2 constellation, allow generating products that provide the required spatial resolution at the local scale (Vanderhoof et al., 2017; Long et al., 2019; Roteta et al., 2019; Hawbaker et al., 2020). However, the operational use of these products in post-fire decision-making and planning is limited to a few countries that invest enough resources to provide this service in a consistent and organized manner immediately after the fire season.

Burned area classification methodologies use all types of spectral indices to identify burned pixels. From spectral vegetation indices such as the Normalized Difference Vegetation Index (NDVI) (Fraser et al., 2000) or the Soil Adjusted Vegetation Index (SAVI), to spectral indices designed to detect burned areas such as the Normalized Burn Ratio (NBR) and its derived indices (Eidenshink et al., 2007; Hawbaker et al., 2017), the Middle Infrared Burned Index (MIRBI) (Trigg and Flasse, 2001) or the Burn Area Index (BAI) (Martín et al., 2006). Each index has shown its ability to detect burned areas in different ecosystems. There is a group of less-used spectral indices, whose formulation is based on trigonometric equations, which calculate the angle of the triangle formed by the spectral response of three consecutive bands (Khanna et al., 2007). In this study, we refer to them as band angle indices (BAnI) (explained in detail in the section "Methodology"). These indices have previously been used to estimate the moisture content of vegetation (Palacios-Orueta et al., 2006; Khanna et al., 2007), detect agricultural residues (Zhang et al., 2014), detect forest pests (Fassnacht et al., 2012), or determine agricultural practices (Tornos et al., 2015). In previous studies, BAnI indices have shown high sensitivity to variations in vegetation moisture content. Therefore, we expect that these indices can provide essential information for the identification of burned areas, since other spectral indices sensitive to vegetation moisture content, such as NBR, have proven to be decisive in identifying and analyzing burned areas (Hawbaker et al., 2017; Giglio et al., 2018). The burned pixel detection capability of some BAnI was studied theoretically by Oliva and Chuvieco (2013) computing separability measures on spectral data from the Medium Resolution Imaginf Spectrometer (MERIS). The authors concluded that the ability to detect burned areas of the BAnI was high when the temporal difference analysis between pre- and post-fire dates was performed. Ramo et al. (2018) consider two BAnI in the initial input set of variables for their machine learning approach. However, the indices were not selected for the algorithm application.

At present, the most widespread approach is to use a combination of indices and spectral bands to obtain the most accurate classification of burned areas and to avoid noise from cloud shadows, the land-water interface, or dark soils (Chuvieco et al., 2019). A set of indices and bands

are introduced in classification algorithms of all kinds, from supervised maximum probability classifications to learning-based classification methods such as neural networks (NN) (Ba et al., 2019), support vector machines (SVMs) (Dragozi et al., 2014), or classification trees (Cabral et al., 2018). The Random Forest (RF) is one of the algorithms based on classification trees that has offered good results in different disciplines, such as land cover classification (Rodriguez-Galiano et al., 2012), biomass estimates (Mutanga et al., 2012; Silveira et al., 2019), or fire severity classification (Collins et al., 2018; Gibson et al., 2020). Regarding burned area mapping, the RF algorithm was successfully applied onn MODIS images (Ramo and Chuvieco, 2017) and Landsat images (Roteta et al., 2021a).

In recent years, the use of the Google Earth Engine (GEE) data processing platform has become widespread, because it allows free access to the entire data archive provided by the space agencies and has a great capacity for data processing, eliminating the need to download the data and the installation of powerful computers or physical servers (Wang et al., 2020). These features have enabled researchers in countries with fewer resources to process and produce official satellite mapping and analyze products (Tsai et al., 2018; Li et al., 2020). In this study, we have developed all the methodology in GEE to make the algorithm easily applicable and transferable, and with the ability to produce burned area maps as quickly as possible.

In Chile, the average annual area burned reported by the country's authorities between 1980 and 2016 was approximately 100,000 ha (CONAF, 2020). However, in January 2017 the area affected by fires exceeded 500,000 ha, triggering a paradigm shift in forest fires in Chile. What happened in 2017 was related to the period of mega-drought occurring in the country (Bowman et al., 2019). Since 2010, the annual rainfall showed a decreasing trend with an average deficit of between 20 and 40% (Garreaud et al., 2020). These drought conditions were expected to continue over time, causing the loss of vegetation and soil moisture, which will favor the formation of large forest fires by increasing the amount of fuel and its flammability (Yebra et al., 2018). These conditions highlight the importance of establishing a system that provides information on burned areas quickly and efficiently in Chile, to be able to act and make decisions as quickly as possible in the face of events of the magnitude of the fires that occurred in 2017 (Jones et al., 2020).

The CONAF (Corporación Nacional Forestal) is the organization in charge of the assessment of the damage produced by the fires. Since the catastrophic fire season of 2017, the CONAF produces fire perimeters for every fire larger than 200 ha by visual interpretation of Landsat satellite images and field data. As that process may be time-consuming, there is special interest in developing an automated burned area product.

This work aims to analyze the contribution of BAn in the classification of burned areas applying a RF algorithm on Sentinel-2 data in order to select the best indices to develop an automated burned area mapping algorithm for all Chile. Even though, the BAnI had shown promise for burned area discrimination in previous studies (Oliva and Chuvieco, 2013), they have not been used in the classification algorithms before. We hypothesized that the information provided by the BAnI would be useful in the discrimination of burned areas as they provide new data and are sensitive to moisture content. We focused on the fires occurred in the Maule region of Chile in the 2017 fire season, as it was the Region with the larger amount of area burned. To carry out this analysis we have designed a two-phase methodology based on the application of the RF algorithm, considering two sets of input variables among which the only difference is the presence or absence of BAnI. Our results were compared to the official fire perimeters produced by CONAF to analyze the performance of the burned area classifications, as well as, with reference perimeters to assess their accuracy. The land cover types classified as burned by the burned area classifications were analyzed to evaluate the most affected land covers and understand where the errors were more common.

Study area

The study area corresponds to the Maule Region (Chile), located approximately between 34.5 and 36.5° latitude (**Figure 1**). This region has a Mediterranean climate of winter rains with variations due to the orography of the area, presenting part of the Andes Mountains to the east.

In 2017, the area affected by forest fires in Chile exceeded all historical values, with damage reaching 570,197 hectares of burnt area (CONAF, 2020). This event received the name Fire Storm and was declared a sixth-generation fire due to its high propagation speed with 114,000 hectares affected in 14 h and intensity of over 30,000 kW/m (CONAF, 2017). The fires were very intense and difficult to control due to the dryness of the vegetation and the weather conditions. Since 2010, central Chile has been affected by severe and prolonged drought conditions (Garreaud et al., 2020), which intensifies the risk of fire and fuel flammability (Yebra et al., 2018). The fire season in Chile expands from November to March. In 2017 fire season the largest fires burned at the same time and were concentrated in January and February.

The Maule region concentrated half of the total burned area in the 2017 fire season (256.000 ha). The most affected land use at the national level was pine forest plantations, of which the largest area is in the Maule region. The second most affected forest type was the Oak–Hualo forest, a formation of native species which concentrates 97% of its total affected area in the Maule region (CONAF, 2020).

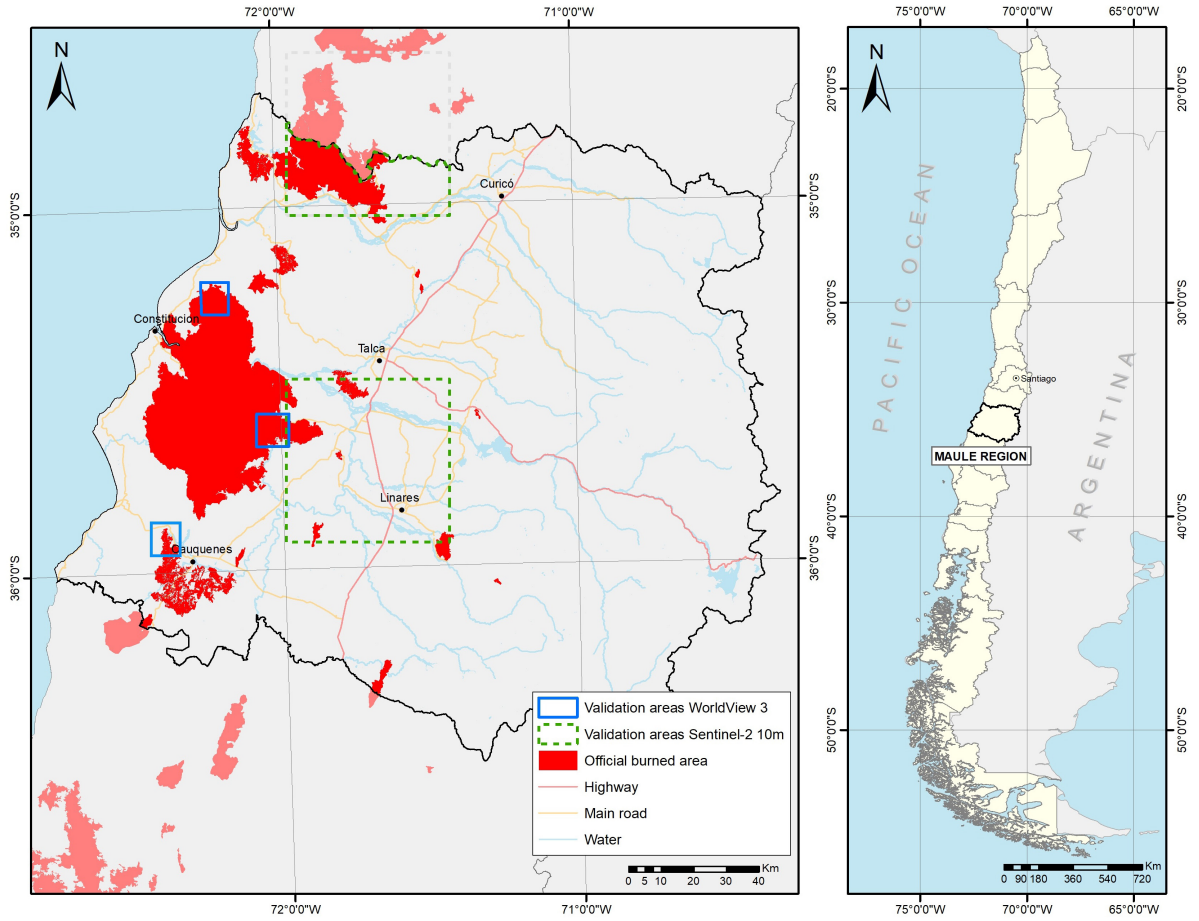

FIGURE 1
Location of the study area: Región del Maule, Chile.

Data

Sentinel-2 data

Data from Level 1C collection Sentinel-2 MultiSpectral Instrument (MSI) belonging to the Copernicus program of the European Space Agency (ESA) was used to develop the burned area classification algorithm. The Sentinel-2 satellite constellation consists of two identical satellites orbiting in parallel (180° apart) at an altitude of 786 km, which allows a global revisit periodicity of 5 days with an acquisition width of 290 km. The images have a spatial resolution ranging from 10 to 60 m in 13 spectral bands (ESA, 2013). In this study, the 20 m resolution bands and the 10 m bands resampled at 20 m were used to perform the classification of burned areas (**Supplementary Table 1**). The level 1C images have radiometric and geometric correction, including orthorectification and spatial registration in a global reference system with sub-pixel precision (ESA, 2013). Sentinel-2 Level 1C images were selected, instead of the atmospherically corrected Level 2A images because the Level 2A images were not available in GEE for the 2016–2017 fire season in Chile at the time of the algorithm development. The earlier date of Sentinel 2A available on GEE at that moment was March 2017, right after the fire season. So, they did not cover the timeframe required for the algorithm.

WorldView 3 data

WorldView 3 (WV3) data was used to obtain the reference perimeters to evaluate the accuracy of the products. WV3 has a high spatial resolution with a pixel size of 1.2 m in the visible and near infrared (NIR) bands and 3.7 m in the shortwave infrared (SWIR) bands. WV3 has three bands in the visible spectral region, one in the Red Edge, two in the NIR, and eight SWIR bands. Being the only high spatial resolution satellite with SWIR bands, WV3 allows the calculation of burned area indices, such as the NBR. The WV3 images are captured by request. They scheduled to capture images from a specific place as the

satellite has the capacity to reposition slightly to capture the required images. The acquired images are then available for purchase on the archive. Due to budget constrains we could only purchase small patches of 10 km × 10 km (100 km^2) from the images available in the archive. That condition posed important limitations as only a portion of the fires were covered by the WV3 acquisitions and none of the areas surrounded the fires were acquired. Therefore, we couldn't select a balanced set of validation areas. Even though, four images covering three sites were used to obtain reference fire perimeters.

Auxiliary data

Two geospatial data files coming from CONAF were used as auxiliary: the vegetational cadaster of the Maule region made in 2013 and the official perimeters of the 2017 fire season. The official fire perimeters were produced by CONAF based on visual interpretation of Landsat satellite images including fires larger than 200 ha (CONAF, 2017). These perimeters were used to generate the random sample of burn and non-burn points needed for the training of the algorithm (more details in section "Burned area classification").

The vegetation cadaster includes detailed information on land use cover with special emphasis on the description of forest stands. The cadaster was used to analyze the land covers affected by the fires. Given the high detail of the classification of vegetation types contained in the cadaster, a reclassification was made to simplify the classification to 7 classes: native forest, shrubland, plantations, grasslands, agricultural, urban areas, and non-burnable areas. The non-burnable category includes rivers, lakes, rocky areas and areas without vegetation, and glaciers.

Methodology

This study performed the classification of the burned area through the application of a RF algorithm. **Figure 2** presents a summary of the methodological workflow followed in this study. First, the images were pre-processed and the spectral indices were computed (see sections "Data pre-processing" and "Spectral indices"). Second, we created multitemporal composites to produce a clear pre-fire and post-fire image (see section "Temporal composites"). Separately, a random sample of burned and non-burned points was generated to train the RF algorithm. Two sets of input variables were created to test the ability of band angle spectral indices (see section "Random forest"). Later, a two-phase classification was applied to the RF-generated probability image to obtain the burned area products (see section "Burned area classification"). Finally, the results were evaluated by comparing them with CONAF official perimeters and with reference data produced from high-resolution images (see section "Accuracy assessment").

Data pre-processing

The Sentinel-2 data was accessed on the cloud processing platform GEE, which allows accessing, analyzing, and processing the data without downloading it. The following processing described was all performed on the GEE platform.

To prepare the images for the following processing water and cloud pixels, which could introduce errors in the results, were filtered out. The permanent water body mask was extracted from the global forest change product generated by Hansen et al. (2013) available in GEE to remove the water pixels, which can be a source of error.

To reduce the effect of clouds and cloud shadows, only images with cloud coverage lower than 20% were including in the processing. In addition, to eliminate cloud pixels, a cloud filter was implemented using the Sentinel-2 QA60 quality band (Hagolle et al., 2010). Due to the generalized classification of cloud types, the information contains some errors related to the presence of low clouds (Nguyen et al., 2020). However, the information on QA60 was useful to eliminate clouds that interfered with the generation of image composites.

Spectral indices

Burned areas have a particular spectral signature which can be identified and highlighted using various spectral indices. Traditional vegetation indices and spectral indices designed specifically for burned areas are widely used in the literature. In this study, we calculated four commonly used indices and three BAnI (**Table 1**).

The BAnI are defined through the trigonometric equations of angle calculation (**Table 1** and **Figure 3**). To calculate them, a triangle shape is drawn in the two-dimensional space that relates the wavelength and the reflectance values of land covers using as vertices the points of three consecutive bands (**Figure 3**; Palacios-Orueta et al., 2006; Khanna et al., 2007). The Shortwave Angle Normalized Index (SANI) and the Shortwave Angle Slope Index (SASI) are based on the relationship between the angle at SWIR 1 (1240 nm, MODIS band 5) and the difference between the reflectances at NIR (865 nm, MODIS band 2) and SWIR 2 (1640 nm, MODIS band 6). However, SANI uses the normalized difference, and SASI the simple difference between the bands. The concept of these indices was built using MODIS bands to assess their ability to discriminate between green vegetation, non-photosynthetic vegetation, and wet and dry soils (Khanna et al., 2007). The β_{SWIR} angle has a higher value in dry soils which decreases in wet and non-photosynthetic vegetation. The higher the moisture the lower the angle. The slope of the line connecting the NIR and SWIR 2 points is positive for dry soils, decreasing as moisture content increases, being close to zero for non-photosynthetic vegetation, and negative for green vegetation (Palacios-Orueta et al., 2006). So,

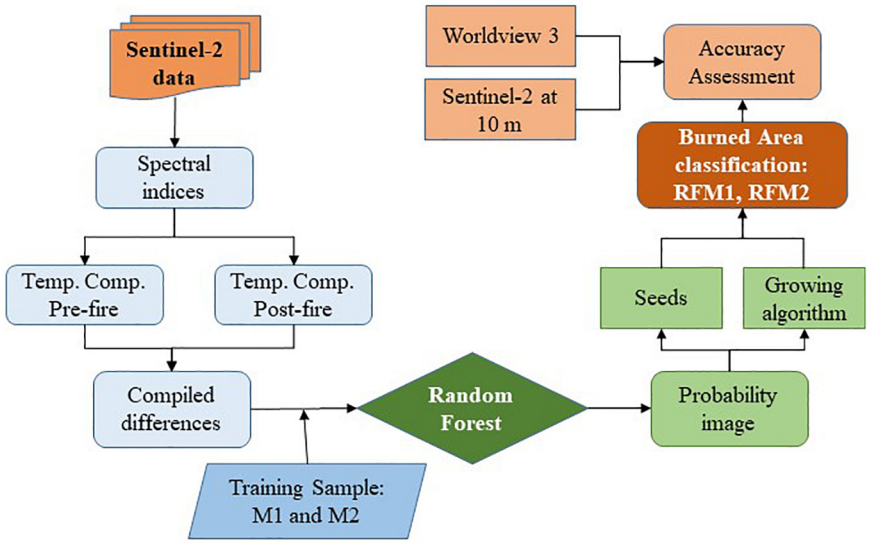

FIGURE 2
Methodological workflow applied in this study to produce burned area classification.

TABLE 1 Equations of spectral indices that were calculated in this study.

Name	Equation	References
Normalized difference vegetation index (NDVI)	$NDVI = \frac{NIR - RED}{NIR+RED}$	Rouse et al., 1974
Normalized burn ratio (NBR)	$NBR = \frac{NIR - lSWIR}{NIR + lSWIR}$	Key and Benson, 2005
Mid InfraRed burn index (MIRBI)	$MIRBI = 10lSWIR - 9.8sSWIR + 2$	Trigg and Flasse, 2001
Soil adjusted vegetation index (SAVI)	$SAVI = (1+L)\frac{NIR - RED}{NIR + RED + L}; L = 0.5$	Huete, 1988
Shortwave angle normalized index (SANI)	$SANI = \beta_{sSWIR} * \frac{lSWIR - NIR}{lSWIR + NIR};$ $\beta_{sSWIR} = cos^{-1}\frac{a^2+b^2-c^2}{2*a*b} radians;$ $a = d_E(NIR,sSWIR);$ $b = d_E(sSWIR,lSWIR);$ $c = d_E(lSWIR,NIR)$	Palacios-Orueta et al., 2006
Shortwave angle slope index (SASI)	$SASI = \beta_{sSWIR} * Slope;$ $Slope = lSWIR - NIR$	Palacios-Orueta et al., 2006
Angle at NIR (ANIR)	$ANIR(\alpha_{NIR}) = cos^{-1}\frac{a^2+b^2-c^2}{2*a*b} radians$ $a = d_E(RED,NIR)$ $b = d_E(NIR,sSWIR)$ $c = d_E(sSWIR,RED)$	Khanna et al., 2007
$d_E = Euclidean\ distance\ by\ wavelength\ and reflectance\ value$		

The details on the Sentinel-2 bands used to calculate these indices are in above table. Reflectance values are used to calculate all indices.

by combining the angle and the slope values the indices show a large range of values separating well different land covers, with high positive values characterizing dry soils and high negative values characterizing healthy vegetation.

However, when translating those indices to Sentinel-2 data the bands used to define the triangle had to be modified because there is no band at 1200 nm. Then, the β_{SWIR} angle had to be centered on band 11 at 1610 nm (short SWIR or sSWIR) in Sentinel-2 data, and the triangle was formed by the NIR band 8A (864 nm), the sSWIR band, and the long SWIR band 12 (2185 nm). The main difference we observed is that the S-2 β_{SWIR} angle did not have as much variation as shown in MODIS β_{SWIR} angle. But the variation of the slope described in the original equation remained. Then, the slope has positive values for dry soils and burned areas and negative values for green vegetation. Consequently, burned areas show high positive values of the SANI and SASI indices in the same range of dry soils, while green vegetation shows negative values.

The angle at NIR (or ANIR index) is centered on the NIR band (**Figure 3**). In its original design (Khanna et al., 2007), the triangle was formed with bands located at Red (659 nm), NIR (865 nm), and SWIR (1240 nm). To apply it to Sentinel-2

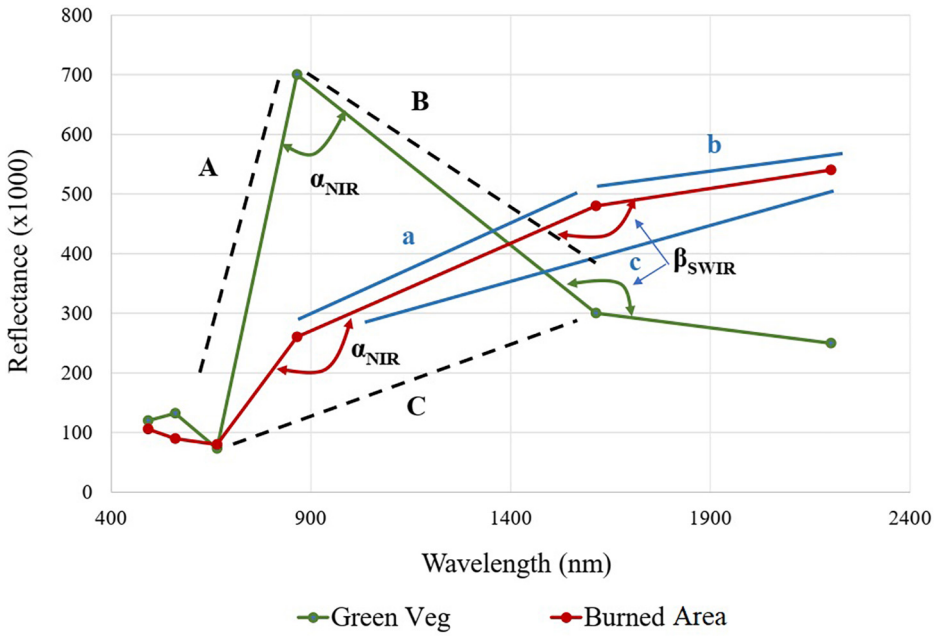

FIGURE 3
Depiction of the equation variables of the band angle indices SANI, SASI, and ANIR. SANI and SASI indices locate in the triangle formed by blue-filled lines **(a–c)** and centered at sSWIR (1610 nm). ANIR index (α_{NIR}) is based on the triangle formed by black dashed lines **(A–C)** and centered at NIR. **(a–c)** Correspond with the nomenclature used in equations in **Table 1** for SANI and SASI indices.

images, we used the sSWIR at 1610 nm as the third vertex. That change in the equation did not affect the results of the ANIR index, since the angle varies from low values characterizing green vegetation and high values characterizing burned areas.

Temporal composites

Temporal composites are created from the images within a date range to eliminate pixels covered by clouds and cloud shadows, which will introduce errors in the classification process, and maximize the differences between non-burned and burned vegetation. The temporal composites were built by applying the criterion of minimizing the NBR value. Then, those pixels with a clearer burned signal were included in the composite, since the lowest NBR values represent the areas more intensely affected by the fire (Roteta et al., 2021a). The values of the bands and indices calculated for the date when the NBR value is the lowest are stored in the composite.

Three date ranges are defined that characterize three situations: pre-fire, active fire, and post-fire. We decided to separate the period of greatest fire activity because the presence of thick smoke remained in the composites and obstructed the observation of the burned area. The periods were considered as follows:

- Pre-fire: 01-October-2016 to 30-November-2016.
- Active fire: 01-December-2016 to 28-February-2017.
- Post-fire: 01-March-2017 to 01-May-2017.

To analyze the changes and classify the burned area that occurred in the fire season, the temporal difference between the pre-fire and post-fire temporal composites was computed.

Random forest

The RF algorithm is one of the most widely used algorithms for the classification of satellite images. Its implementation has been successful in various fields such as land cover classification (Rodriguez-Galiano et al., 2012), biomass estimates (Mutanga et al., 2012; Silveira et al., 2019), fire severity classification (Collins et al., 2018; Gibson et al., 2020) and discrimination of burned areas (Ramo and Chuvieco, 2017), among others. This algorithm is based on decision trees, which divide the data sample binary, by applying rules to the input variables until each of the pixels is assigned to the established classes (Breiman, 2017).

Random forest generates a number of decision trees indicated by the user, which are calibrated using a subset of the training data randomly selected for each decision tree. The algorithm then analyzes the results obtained from each of the generated decision trees and assigns to each pixel a probability of belonging to one of the established categories (Breiman, 2001).

These probability values are the result of the application of the RF algorithm.

The operation of the RF is defined by the number of decision trees calculated, the number of leaves or levels to be calculated, and the representativeness of the training sample. Studies have shown that increasing the number of decision trees calculated improves the final precision of the classification. But this value reaches a saturation point from which the result does not improve when a new decision tree is added, affecting negatively the final performance of the classification (Rodriguez-Galiano et al., 2012). Therefore, it is recommended to choose the number of iterations that allow the best and most computationally efficient result (Breiman, 2017).

To train the RF algorithm for burned area classification we need a training sample containing burned and unburned pixels. Two sets of 15,000 points were randomly generated, one in the burned areas delimited by CONAF official perimeters, and the other in the unburned areas of the entire Maule Region. The random points classified as burned had to be visually checked because the CONAF perimeters consider as burned areas some unburned inner islands, and the rivers that cross the fires. This issue was detected in early versions of the results and was solved by removing the points that were not assigned to the proper class.

In this study, two training samples were generated according to the variables considered.

- In the first sample (referred to as M1), we included the temporal difference of the 6 spectral bands and the dNDVI, dSAVI, dNBR, and dMIRBI indices.
- In the second sample (referred to as M2), we included the bands and indices of M1, also adding the temporal difference of the BAnI, dSANI, dSASI, and dANIR.

Each training sample was used for the calibration of the RF algorithm. We established a maximum of 40 decision tree iterations and 10 leaves or nodes per decision tree.

Burned area classification

The final burned area classification is computed by applying a two-phase methodology on the output probability image of the RF algorithm, which is a widely used methodology for the classification of burned area as it efficiently balances omission and commission errors (Bastarrika et al., 2011; Chuvieco et al., 2016). This methodology consists of a first phase where the pixels with a higher probability of being burned (also called seed pixels) are selected. The second phase, also called the growth phase, uses a laxer threshold to establish the final delimitation of the burned area. In this study, we selected as seed pixels those that have a probability greater than 90% of being burned. For the growth phase, the Otsu method was applied. The Otsu method allows us to segment the image into two categories. It is based on the statistical analysis of the histogram of the image which determines the point where the separation valley between the two peaks of the frequency distribution of pixels belonging to burned and unburned classes occurs (Otsu, 1979). This method offers as a result a value in which both distributions can be separated, which was applied to the probability image to determine the perimeter of the burned area. Finally, the patches of pixels selected for the final burned area product are those obtained from the application of the Otsu method that contains at least one seed pixel and has an area greater than 10 ha.

Accuracy assessment

Reference perimeters

To determine the degree of error associated with the product obtained from the RF algorithm using the two training samples, we generated two sets of reference perimeters (**Table 2**). First, the burned areas on three 10 km × 10 km WV3 post-fire images were digitized. WV3 has a high spatial resolution satellite with a pixel size of 1.2 m in the visible and NIR bands and 3.7 m in the SWIR bands. Being the only high spatial resolution satellite with SWIR bands, WV3 allows the calculation of burned area indices. However, as our purpose was to obtain reference perimeters with the highest spatial resolution, the digital delineation of the burned area polygons was performed on the higher resolution bands using color composites and the NDVI to discriminate them.

Also, reference burned perimeters were obtained from two 50 km × 50 km areas on Sentinel-2 images at 10 m using the Roteta et al. (2021a) reference perimeter tool (RPT) built on GEE. The RPT is a classification tool that allows the semi-automatical classification of the burned area using a pair of Sentinel-2 or Landsat images. The RPT applies an RF model using as inputs manually digitized burned and unburned polygons within the GEE map. The results are exported in ESRI shapefile format, which complies with CEOS' BA assessment protocol (Boschetti et al., 2009). One of the sites was clipped to cover only the extent of the Maule Region, even though the whole 50 km × 50 km validation site was classified. Long temporal reference units (Franquesa et al., 2022) considering the same post-fire date window established for the temporal composites created (see section "Temporal composites") were used to ensure the reference perimeters could be used for the validation of the BA classification (see **Table 2**).

Confusion matrix and accuracy measures

To quantify the accuracy of our burn area classification, errors of commission and omission were calculated, as well as the overall accuracy of the classification (Padilla et al., 2015). We used as reference perimeters the burned areas obtained from

TABLE 2 Satellite data used to obtain the reference perimeters of burned area.

Validation area	Date	Image reference	Size of the validation area	Spatial resolution
Site 1	19-February-2017	WorldView 3	10 km × 10 km	1.2 m
Site 2	Pre-fire: 10-January-2017	WorldView 3	10 km × 10 km	1.2 m
	Post-fire: 07-February-2017	WorldView 3	10 km × 10 km	1.2 m
Site 3	01-February-2017	WorldView 3	10 km × 10 km	1.2 m
Site 4	Pre-fire: 10-November-2016	Sentinel-2	50 km × 20 km	10 m
	Post-fire: 20-December-2016	Sentinel-2	50 km × 20 km	10 m
Site 5	Pre-fire: 30-November-2016	Sentinel-2	50 km × 50 km	10 m
	Post-fire: 20-December-2016	Sentinel-2	50 km × 50 km	10 m

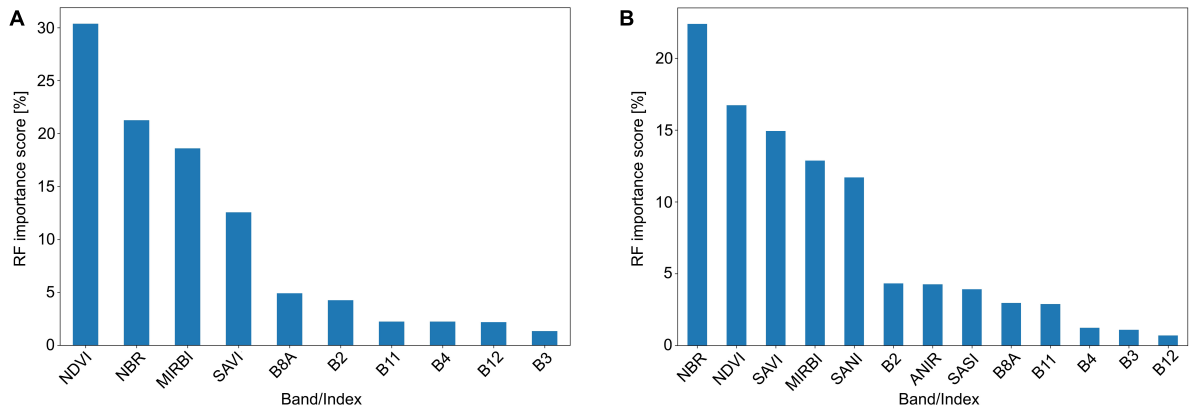

FIGURE 4
Random forest importance index of each of the variables included in the algorithm calibration. **(A)** Importance index of M1, **(B)** importance index of M2.

the WV3 and Sentinel-2 images. In that way, we have accuracy measures at different scales covering variable scenarios within the Maule region.

Results

Burned area classification

As our main objective was to determine if the BAnI would contribute to the discrimination of BA using an RF classifier, we computed the importance index produced after the calibration of the two RF algorithms (Figure 4). We observed that both RF algorithms have the same four indices with the highest importance values, although in a different order. It is in the fifth position where the SANI index shows an importance index value higher than the fifth variable of the RF_{M1} algorithm. ANIR and SASI indices also appear to contribute to the classification located in seventh and eighth place, respectively.

The application of the RF algorithm using the two sets of variables offered different classifications of burned area (Table 3). The burned area produced by the sample set M1 (referred to as RF_{M1}) classified the largest amount of burned area, with a total of 318,937 ha, while the classification produced by the second set of variables (RF_{M2}) obtained a total of 309,068.6 ha. When comparing the two results with CONAF data, it can be seen the greatest differences are concentrated in the coverage of agricultural land, forest plantation, and shrubland (Table 3). The RF_{M1} result is the one that classifies more native forest area and agricultural use as burned.

To highlight the different spatial distribution of the three burned area classifications, we present in Figure 5 the overlapped area of the three burned area maps. The two classifications RF_{M1} and RF_{M2} detected the large fires identified by CONAF, delimiting them in detail. In the larger burned areas, we observed some unburned areas inside the burned perimeters that were classified as burned by CONAF. The RF_{M1} classifies a large area as burned in the central and northern zone of the region situated on agricultural land use. However, those areas were visually identified as a commission error. On the other hand, the RF_{M2} classification presents a concentration of burned area in agricultural land use located in the south of the region. Through a visual inspection of the results, we concluded that the areas correctly classified as burned in agricultural use are those areas registered by both classifications (represented in purple color in Figure 5). While

TABLE 3 Distribution of burned area in hectares by type of land cover in each of the classifications of the burned area obtained and in the official delimitation the category "overlapped" includes the burned area that coincides in the three classifications (RF_{M1}, RF_{M2}, and CONAF).

Land cover	CONAF	RF_{M1}	RF_{M2}	Overlapped area
Forest plantation	186,396.84	174,556.91	178,670.96	165,267.21
Shrubland	57,111.60	63,646.09	63,466.37	49,786.58
Sclerophyll native forest	23,393.23	26,823.96	24,598.52	20,250.46
Agricultural areas	13,762.79	48,606.61	36,391.06	11,260.85
Grasslands	3,502.04	4,814.32	5,478.20	2,747.08
Unburnable	1,507.02	0	0	0.00
Urban areas	266.18	290.74	267.92	208.32
Not classified	110.95	198.37	195.58	94.39
Total	286,050.6	318,937.00	309,068.6	249,614.8

the burned areas classified only by one product are in most cases errors of commission (represented in blue and yellow color in Figure 5).

The area where the three burned area maps overlapped focused on the larger fires that occurred in the region. However, we found it interesting to analyze the areas where only one of the BA products classified them as burned and the areas where two of the products overlapped. By analyzing those areas, we observed which were the land covers with higher differences and where the errors might be located (Figure 6). In the case of the forest plantation cover, CONAF perimeters classified as BA more than 12,000 ha that were not classified by any RF classification, indicating that the area might be related to an overestimation of the BA due to an oversimplification of the fire perimeter. There are also areas classified as burned only by one of the RF classifications and their paired combinations, these types of differences are concentrated at the edges of the burned areas. In shrubland, the overlap between RF_{M1} and RF_{M2} showed a higher value, indicating that both RF classifications are mapping the smaller fires occurring mainly in shrubland and grassland. On the other hand, the classification RF_{M1} classified a larger area in sclerophyll forest. In the Supplementary Figures 1, 2 we can observe how RF_{M1} shows a higher number of burned areas classified in the Eastern part of the Region (around the 71° longitude line) corresponding to native forest. We revised those areas visually and confirmed that they were areas affected by the shadow of the relief, then they were commission errors. That is a common error in burned area classification (Garcıa and Chuvieco, 2004) and we expected to encounter this type of error as the Andean Mountain range has a very irregular and steep relief. Therefore, RF_{M1} presented more commission error than RF_{M2} not only in agricultural areas but also in the native forest located in the Andes.

The analysis of the agricultural areas highlights the implications of leaving out agricultural fires from the BA statistics. As CONAF does not include small (<200 ha) and agricultural fires in the official fire perimeters reported, it was expected that the BA classified by CONAF was less than the RF classifications. We also noticed the differences in the area classified as burned by both RF_{M1} and RF_{M2} and by only one of them. Both classifications coincide on almost 16,000 ha burned on agricultural land, while RF_{M1} and RF_{M2} added up 21,000 ha more and 8,500 ha, respectively. As we presented in Figure 5, the area classified as burned in both RF classifications showed distinct spatial distribution, particularly in agricultural land. So, each classification is sensitive to different spectral conditions. However, if we consider as correct the burned area classified in agricultural land by both RF classifications, RF_{M1} shows three times more area wrongly classified than RF_{M2}.

Accuracy analysis

The accuracy analysis showed the high accuracy of the BA classifications produced with the RF_{M1} and RF_{M2} algorithms (Table 4). The errors obtained at a local scale from the WV3 images were lower than 6 % in all cases. In that analysis, the error balancing of both classifications was alternated, as RF_{M1} showed a lower commission error than RF_{M2} and RF_{M2} showed a lower omission error than RF_{M1}. In the case of the accuracy analysis performed with Sentinel-2 images, the RF_{M2} offered lower omission and commission errors than RF_{M1}, which is related to the lower BA classified in agricultural areas than RF_{M1}. In this case, we observed more clearly the improvement of the BA classification as a consequence of including the BAnI in the set of input variables.

Discussion

Contribution of band angle indices to the classification of burned areas

We trained two RF algorithms using two sets of input variables. RF_{M1} included the temporal differences of the six spectral bands of Sentinel-2 at 20 m and the indices NDVI, SAVI, NBR, and MIRBI. On the other hand, RF_{M2} added to the input variables in M1 three BAnI. The results showed the different classifications produced by both algorithms. The importance index values showed the contribution of the SANI to the classification algorithm was on the same level as MIRBI (Figure 4), proving that SANI adds new information to the algorithm. The SANI index was not designed for burned area mapping. However, the range of values offered

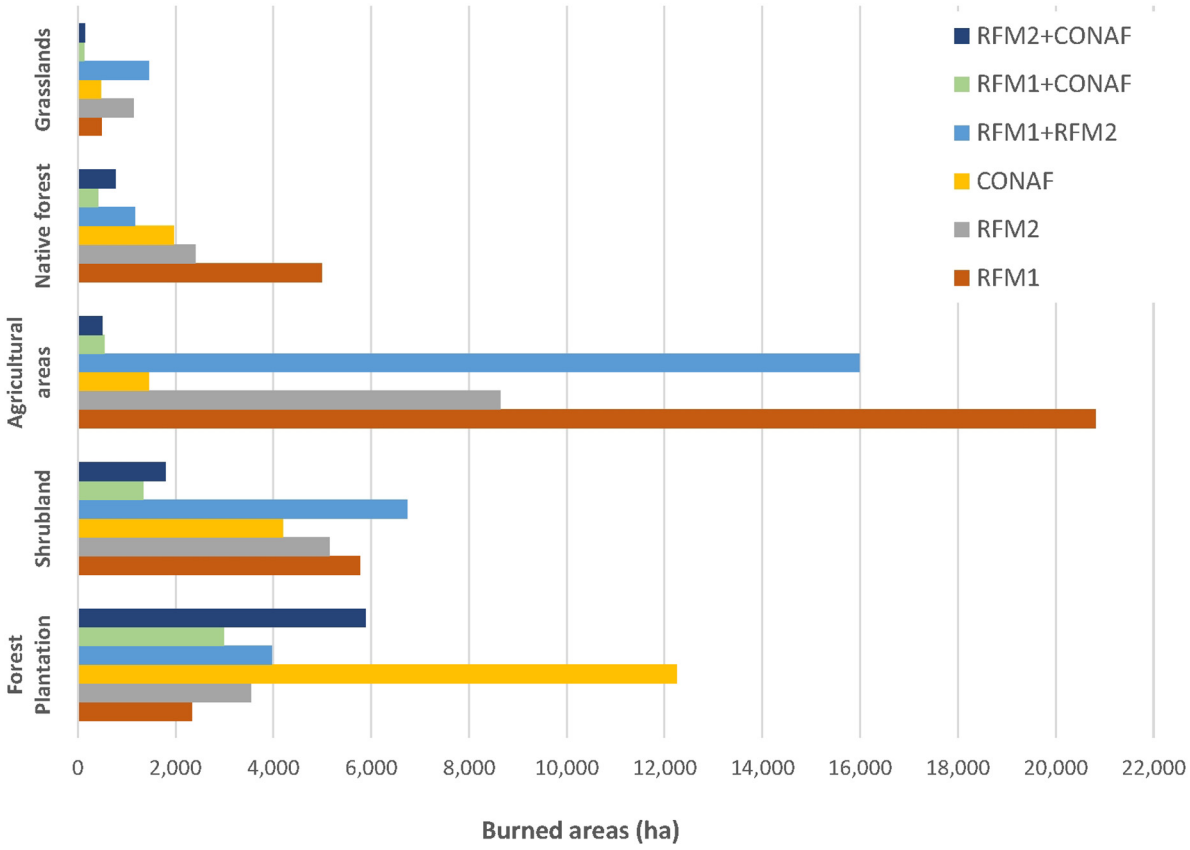

FIGURE 5
Spatial distribution of the comparative analysis between the three burned area products: Official CONAF source, and RF_{M1} and RF_{M2} classifications.

by the SANI can help discriminate between green vegetation, non-photosynthetic vegetation, and wet and dry soils, where high positive values characterize dry soils and high negative values describe healthy vegetation (Palacios-Orueta et al., 2006). We identified as commission errors the burned areas classified in agricultural land in the north of the Maule region by the RF_{M1} BA classification, which translated into an overestimation of 78% regarding agricultural burning. The BAnI improved the BA classification as the RF_{M2} showed fewer commission errors in agricultural areas and lower omission errors related to the classification of BA at the edge of the fire (**Figure 5**).

Numerous studies have explored the use of different spectral indices to detect burned areas, from vegetation indices such as the NDVI, the GEMI, or the EVI, to indices designed to be sensitive to the post-fire signal like the BAI, the MIRBI, or the NBR (Martín et al., 2006; Loboda et al., 2007; Veraverbeke et al., 2011; Bastarrika et al., 2014; Lizundia-Loiola et al., 2020; Smiraglia et al., 2020; Koutsias and Pleniou, 2021). Those indices exploit the spectral change resulting from vegetation removal, which involves decreasing the near-infrared (NIR) reflectance and increasing the SWIR reflectance. Since the SANI index uses the NIR and the SWIR bands, it is also sensible to the post-fire spectral change. SANI combines the normalized difference of the short SWIR (sSWIR) and NIR with the angle centered at the sSWIR band. The normalized index is negative for green vegetation and positive for burned areas, and the angle β_{SWIR} has a higher value in burned areas and dry soils. Although the indices exploit the same spectral relationship, their different formulation makes them unique, and each of them offers information to discriminate burned areas. Because of that, complex models and algorithms based on machine learning, which work with a high number of input variables, are spreading widely, such as the SVM, the NN, and the RF. Ramo et al. (2018) evaluated those three algorithms for burned area mapping on a global scale, obtaining the best results with the RF classifier. Ramo et al. (2018) introduced the SASI and ANIR indices into the initial set of input variables. The SASI and ANIR were selected by the RF and regression methods for variable selection, but they were not selected for the final set of variables used. Our results support the findings of Ramo et al. (2018), as the temporal difference of SASI and ANIR indices did not show a high importance index value in the RF_{M2} algorithm.

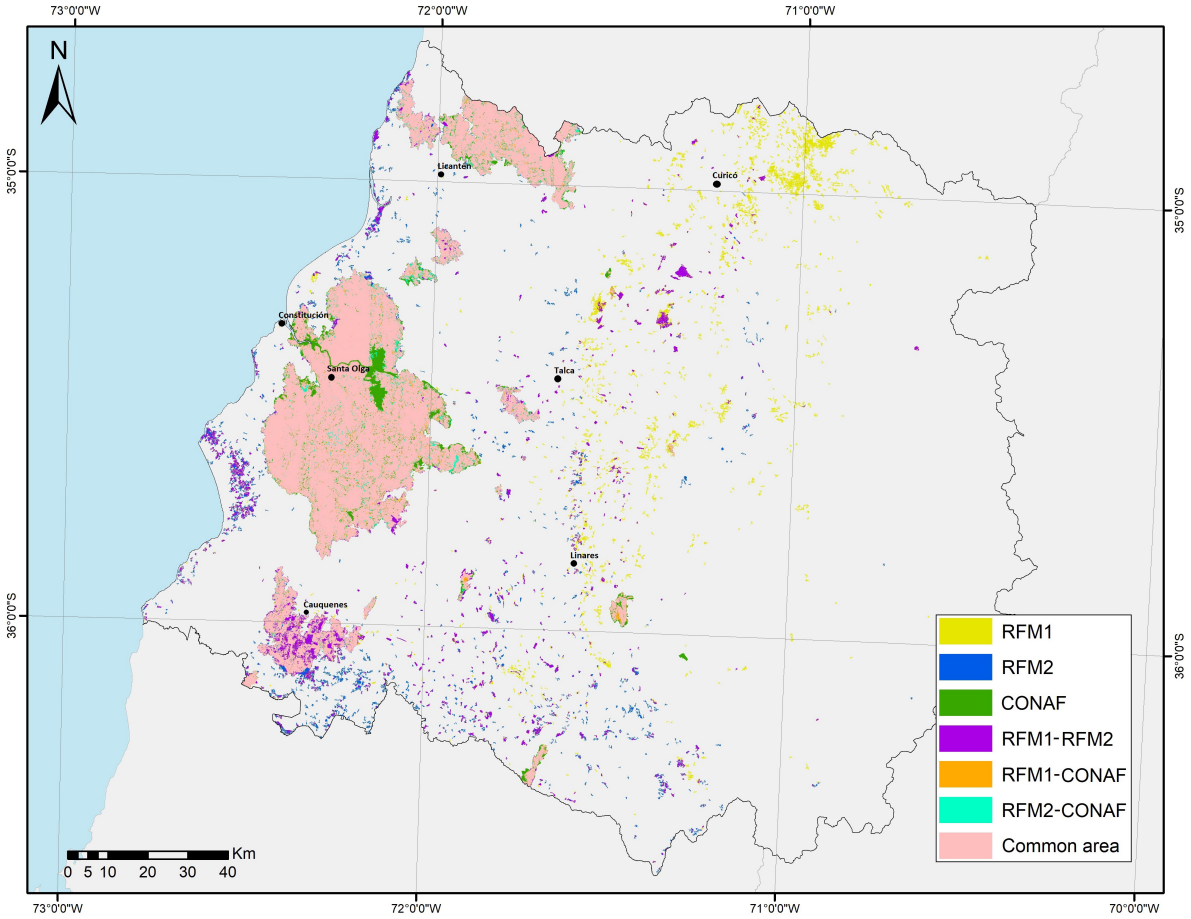

FIGURE 6
Comparative analysis of the classification of the burned area generated by the two results of the Random Forest algorithm, RF_{M1} and RF_{M2}, the official CONAF perimeters, and the areas where two of the burned area maps overlapped. Only the land covers with the greater differences are represented.

TABLE 4 Accuracy analysis results obtained at 1.2 m spatial resolution from the WV3 images and 10 m resolution from the Sentinel-2 reference perimeters.

	WV3 ref. perimeters		Sentinel-2 (10 m) ref. perimeters	
	RF_{M1}	RF_{M2}	RF_{M1}	RF_{M2}
Omission error (%)	5.86	4.41	7.64	4.97
Commission error (%)	4.58	5.95	21.42	17.82
Overall accuracy (%)	92.03	91.97	95.66	96.62

Algorithm performance

We validated our classification results using reference perimeters obtained from two datasets at different spatial resolutions. First, we derived reference perimeters from three high-resolution WV3 images covering 100 km^2 each. The images' location and date were constrained by the availability of images in the archive since they were acquired on demand. The three validation areas were mainly centered on the big fires present in the region. So, the validation results of these areas offer a good estimation of the accuracy of the classifications regarding the burned area delineation. We obtained similar omission and commission errors for both classifications ranging between 4 and 6%, meaning that both BA products produced highly accurate BA mapping.

However, those validation sites covered a small proportion of the region's surface. To properly assess the performance of the BA classifications in different land covers, we obtained reference perimeters by applying the RPT (Roteta et al., 2021a) on two sites of 50 km × 50 km using Sentinel-2 images at 10 m. In this case, one of the validation sites covers part of the agricultural area in the region, and the other extends over a large fire situated in the north of the region. The omission errors (7.6% for RF_{M1} and 5% for RF_{M2}) were lower than the errors reported in previous studies using Sentinel-2 images for BA mapping. On the other hand, the commission errors (21.4% for RF_{M1}

and 17.8% for RF_{M2}) were within the range of values found in other studies (Ramo et al., 2018). Comparatively, Ramo et al. (2018), who applied an optimized machine learning approach, reported a range of omission and commission errors in the Mediterranean and temperate forests of 21–59 and 11–27%, respectively. Seydi et al. (2021) applied several classification algorithms to Sentinel-2 data to classify BA, obtaining the best results from an RF classifier with an optimal selection of input variables, showing errors of omission and commission of 9.21 and 8.74%, respectively.

Comparing our results with the BA products derived from Landsat data at 30 m spatial resolution, our classifications were highly accurate for BA delimitation at the local level, improving previous studies' results (Mallinis and Koutsias, 2012; Hawbaker et al., 2020). At larger scales, our results also showed lower omission and commission errors (Vanderhoof et al., 2017; Hawbaker et al., 2020; Roteta et al., 2021b). Roteta et al. (2021a) offered a conservative classification method as they showed lower commission than omission errors, so they missed burned areas in their classification. On the contrary, we obtained a higher commission than omission errors. Therefore, our BA classification delineates the BA precisely at the expense of producing false detections (Padilla et al., 2015).

We analyzed in detail which land covers presented higher omission and commission errors. **Figure 7** shows the correspondence between the validation analysis and the land covers affected in one of the validation areas, although we performed the analysis in both validation sites. In general, in both RF classifications, the omission errors were concentrated in small patches of shrubland and on the edge of the large fires, where shrubland or native forest was present. On the other hand, the commission errors are mainly related to agricultural areas where the spectral signal of harvested areas was confused with the spectral signal of burned areas.

Comparing both RF classifications, we observed clear differences in the spatial distribution of the errors, and lower omission and commission errors in RF_{M2} (as presented in **Table 4**). RF_{M2} presented lower commission errors in agricultural areas and classified a higher number of small patches of shrubland as BA. Therefore, the RF_{M2} classifier, which included the BAnI, showed improved performance over the RF_{M1}.

The importance of agricultural and small burned areas

Observing the comparison of the three BA maps (**Figure 5**), we found important differences between the area officially reported by the National Agency CONAF and the two BA classifications. The reasons were related to the characteristics of the product itself. First, the official reports include only forest fires larger than 200 ha, hence the omission of small fires. Consequently, that condition generates an underestimation of 7.6% of the actual area burned between January and March 2017. However, CONAF's fire perimeters also overestimate the extent of the burned area because they classified as BA some unburned areas inside the fire perimeters (7% of CONAF BA). In this case, the under and overestimation balanced out, and the total BA offered by CONAF did not differ much from the values obtained from the satellite image classification. Even though in this study case the contribution of smaller fires is minimal due to the large fires in the Region, it is important to consider BA smaller than 200 ha since they have an important impact on the estimation of emissions released by the fires (Randerson et al., 2012; Roteta et al., 2019; Ramo et al., 2021).

Second, the official perimeters only consider fires affecting forested areas. Then, the agricultural fires are never going to be included in their reports. We considered agricultural burns the croplands classified as BA by both RF algorithms, which means 5% of the burned areas will be underreported (**Figure 6**). These numbers are in line with previous studies that highlighted the importance of reporting the area burned in agricultural land (Hall et al., 2021) and of considering the implications of cropland expansion through burning (Noojipady et al., 2017).

The use of Google Earth Engine to produce cost-efficient BA products

Google Earth Engine proved to be a valuable tool for BA detection at the regional scale. The study area of the Maule region contained 200 Sentinel-2 scenes for the 7 analyzed months, which would have meant downloading and processing around 130 GB of data if this was done in a local system. Instead, the whole process was carried out virtually in the GEE platform, taking advantage of its available datasets, which allowed fast BA detection and no need for the authors to manage heavy data. Along with its satellite imagery datasets, the platform also contains a wide variety of methods and algorithms for data processing, including the RF classifier used in this study, which enabled an accurate BA detection based on several spectral bands and indices. Since this classification algorithm was applied in a small area and the RF training samples could be obtained beforehand, the GEE processing consisted mainly in classifying S2 images, allowing a faster BA detection since the whole area was processed in just 15 min. This contrasts with several other studies in GEE that first require obtaining burned and unburned samples locally adapted to the processed area in each case, either by supervised training or by a series of thresholds and conditions (Daldegan et al., 2019; Roteta et al., 2021a,b; Seydi et al., 2021), making the process much slower. Even so, RF training samples have already been collected beforehand in some studies, even at the continental or global scale (Long et al., 2019; Sulova and Jokar Arsanjani, 2020).

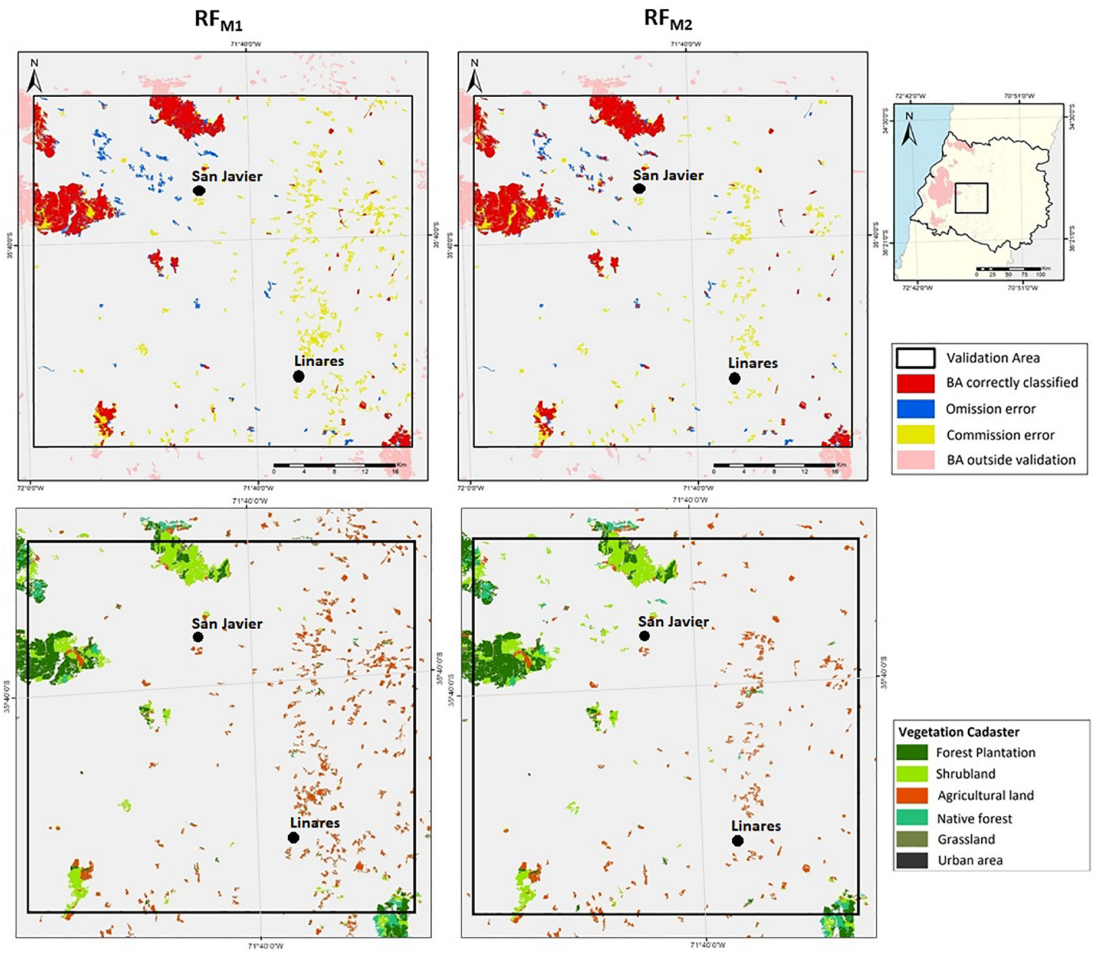

FIGURE 7
On the top, evaluation of the omission and commission errors produced by the two burned area classification algorithms. On the bottom, land covers classified as burned areas by the two burned area classification algorithms are shown.

Conclusion

In this study, we developed two RF algorithms for burned area mapping on GEE using two different sets of input variables in the Maule Region (Chile). We used two different sets of input variables because we wanted to test the capabilities of BAnI for detecting burned areas. From the three BAnI used, the SANI index proved to provide significant information for the discrimination of BA, since it was selected as a variable of high importance in the RF model. Our results showed improved BA classification accuracy from the RF_{M2} classification, which included as input the three BAnI. RF_{M2} offered very low omission errors (5%) and commission errors in the range of previous studies (17%). The commission errors were mainly related to the erroneous classification of agricultural land as BA, due to the similar spectral signal generated after harvesting. The BA classifications performed in this study were computed using GEE, which allowed the processing of hundreds of satellite images without downloading the data and provided the processing capability to calibrate and apply the classification algorithms. The generation of these burned area products is much less time-consuming than manually digitizing the burned area perimeters in each satellite image. In addition, the results offered by the BA classifications included fires smaller than 200 ha and agricultural fires, which are not considered in the official statistics.

Data availability statement

The datasets produced in this study will be shared upon request to the corresponding author. The codes developed and the assets needed to run the algorithm are listed below: Code: https://code.earthengine.google.com/ae6aa079ae39ebd8353cf30b21d54b5a.

Assets: https://code.earthengine.google.com/?asset=users/roxanamansillap/articulo_titulo/REGION_C17_proj, https://code.earthengine.google.com/?asset=users/roxanamansillap/articulo_titulo/cuadro_reg, https://code.earthengine.google.com/?asset=users/roxanamansillap/articulo_titulo/pq, https://code.earthengine.google.com/?asset=users/roxanamansillap/articulo_titulo/ptos_noquem, https://code.earthengine.google.com/?asset=users/roxanamansillap/articulo_titulo/ptos_quem, and https://code.earthengine.google.com/?asset=users/roxanamansillap/articulo_titulo/ptos_quem_mov.

Author contributions

PO led the writing of the manuscript, organized the results and the discussion sections, and prepared the manuscript for publication. RM wrote and applied the GEE code and performed the accuracy assessment. ER helped with the coding of the algorithm and provided the GEE code for the generation of reference perimeters. WP-M revised the manuscript and checked the quality of the figures. All authors contributed to discussing and revising the manuscript.

Funding

This study was funded by the Chilean Association for Research and Development (ANID) with the research grant FONDECYT Iniciacion 11181331.

Acknowledgments

We thank CONAF for the fire perimeters facilitated and for the fruitful discussions about the fires of 2017 in Chile.

Conflict of interest

The authors declare that the research was conducted in the absence of any commercial or financial relationships that could be construed as a potential conflict of interest.

Publisher's note

Supplementary material

The Supplementary Material for this article can be found online at: https://www.frontiersin.org/articles/10.3389/ffgc.2022.1052299/full#supplementary-material

References

Ba, R., Song, W. G., Li, X. L., Xie, Z. X., and Lo, S. M. (2019). Integration of multiple spectral indices and a neural network for burned area mapping based on MODIS data. *Remote Sens.* 11:326. doi: 10.3390/rs11030326

Bastarrika, A., Alvarado, M., Artano, K., Martinez, M. P., Mesanza, A., Torre, L., et al. (2014). BAMS: A tool for supervised burned area mapping using Landsat data. *Remote Sens.* 6, 12360–12380. doi: 10.3390/rs61212360

Bastarrika, A., Chuvieco, E., and Martín, M. P. (2011). Mapping burned areas from Landsat TM/ETM+ data with a two-phase algorithm: Balancing omission and commission errors. *Remote Sens. Environ.* 115, 1003–1012. doi: 10.1016/j.rse.2010.12.005

Benali, A., Mota, B., Carvalhais, N., Oom, D., Miller, L. M., Campagnolo, M. L., et al. (2017). Bimodal fire regimes unveil a global-scale anthropogenic fingerprint. *Glob. Ecol. Biogeogr.* 26, 799–811. doi: 10.1111/geb.12586

Boschetti, L., Roy, D. P., Justice, C. O., and Humber, M. L. (2015). MODIS-Landsat fusion for large area 30 m burned area mapping. *Remote Sens. Environ.* 161, 27–42. doi: 10.1016/j.rse.2015.01.022

Boschetti, L., Roy, D., and Justice, C. (2009). *International Global Burned Area Satellite Product Validation Protocol. Part I–production and standardization of validation reference data*. (Silver Spring, MD: Committee on Earth Observation Satellites), 1–11.

Bowman, D. M., Kolden, C. A., Abatzoglou, J. T., Johnston, F. H., Van Der Werf, G. R., and Flannigan, M. (2020). Vegetation fires in the Anthropocene. *Nat. Rev. Earth Environ.* 1, 500–515. doi: 10.1038/s43017-020-0085-3

Bowman, D., Moreira-Munoz, A., Kolden, C. A., Chavez, R. O., Munoz, A. A., Salinas, F., et al. (2019). Human-environmental drivers and impacts of the globally extreme 2017 Chilean fires. *Ambio* 48, 350–362. doi: 10.1007/s13280-018-1084-1

Breiman, L. (2001). Random forests. *Mach. Learn.* 45, 5–32. doi: 10.1023/A:1010933404324

Breiman, L. (2017). *Classification and regression trees*. New York, NY: Routledge. doi: 10.1201/9781315139470

Cabral, A. I. R., Silva, S., Silva, P. C., Vanneschi, L., and Vasconcelos, M. J. (2018). Burned area estimations derived from Landsat ETM plus and OLI data: Comparing genetic programming with maximum likelihood and classification and regression trees. *ISPRS J. Photogramm. Remote Sens.* 142, 94–105. doi: 10.1016/j.isprsjprs.2018.05.007

Chuvieco, E., Lizundia-Loiola, J., Pettinari, M. L., Ramo, R., Padilla, M., Tansey, K., et al. (2018). Generation and analysis of a new global burned area product based on MODIS 250 m reflectance bands and thermal anomalies. *Earth Syst. Sci. Data* 10, 2015–2031. doi: 10.5194/essd-10-2015-2018

Chuvieco, E., Mouillot, F., Van Der Werf, G. R., San Miguel, J., Tanase, M., Koutsias, N., et al. (2019). Historical background and current developments for mapping burned area from satellite Earth observation. *Remote Sens. Environ.* 225, 45–64. doi: 10.1016/j.rse.2019.02.013

Chuvieco, E., Pettinari, M. L., Koutsias, N., Forkel, M., Hantson, S., and Turco, M. (2021). Human and climate drivers of global biomass burning variability. *Sci. Total Environ.* 779:146361. doi: 10.1016/j.scitotenv.2021.146361

Chuvieco, E., Yue, C., Heil, A., Mouillot, F., Alonso-Canas, I., Padilla, M., et al. (2016). A new global burned area product for climate assessment of fire impacts. *Glob. Ecol. Biogeogr.* 25, 619–629. doi: 10.1111/geb.12440

Collins, L., Griffioen, P., Newell, G., and Mellor, A. (2018). The utility of Random Forests for wildfire severity mapping. *Remote Sens. Environ.*216, 374–384. doi: 10.1016/j.rse.2018.07.005

CONAF (2017). *Análisis de la afectación y severidad de los incendios forestales ocurridos en enero y febrero de 2017 sobre los usos de suelo y los ecosistemas naturales presentes entre las regiones de Coquimbo y la Auracanía de Chile. Informe Técnico*. Santiago: CONAF.

CONAF, (2020). Estadísticas - Resumen Nacional Ocurrencia (Número) y Daño (Superficie afectada) por incendios forestales 1977-2020". 07/2020 ed. Available online at: https://www.conaf.cl/incendios-forestales/incendios-forestales-en-chile/estadisticas-historicas/: CONAF (accessed August 12, 2022).

Daldegan, G. A., Roberts, D. A., and Ribeiro, F. D. F. (2019). Spectral mixture analysis in Google Earth Engine to model and delineate fire scars over a large extent and a long time-series in a rainforest-savanna transition zone. *Remote Sens. Environ.* 232:111340. doi: 10.1016/j.rse.2019.111340

Dragozi, E., Gitas, I. Z., Stavrakoudis, D. G., and Theocharis, J. B. (2014). Burned area mapping using support vector machines and the FuzCoC Feature Selection Method on VHR IKONOS Imagery. *Remote Sens.* 6, 12005–12036. doi: 10.3390/rs61212005

Eidenshink, J., Schwind, B., Brewer, K., Zhu, Z.-L., Quayle, B., and Howard, S. (2007). A project for monitoring trends in burn severity. *Fire Ecol.* 3, 3–21. doi: 10.4996/fireecology.0301003

ESA (2013). *Sentinel-2 User Handbook*, ed. B. Hoersch (Paris: European Space Agency).

Fassnacht, F. E., Latifi, H., and Koch, B. (2012). An angular vegetation index for imaging spectroscopy data—Preliminary results on forest damage detection in the Bavarian National Park, Germany. *Int. J. Appl. Earth Observ. Geoinform.* 19, 308–321. doi: 10.1016/j.jag.2012.05.018

Franquesa, M., Lizundia-Loiola, J., Stehman, S. V., and Chuvieco, E. (2022). Using long temporal reference units to assess the spatial accuracy of global satellite-derived burned area products. *Remote Sens. Environ.* 269:112823. doi: 10.1016/j.rse.2021.112823

Fraser, R., Li, Z., and Cihlar, J. (2000). Hotspot and NDVI differencing synergy (HANDS): A new technique for burned area mapping over boreal forest. *Remote Sens. Environ.* 74, 362–376. doi: 10.1016/S0034-4257(00)00078-X

Garcıa, M., and Chuvieco, E. (2004). Assessment of the potential of SAC-C/MMRS imagery for mapping burned areas in Spain. *Remote Sens. Environ.* 92, 414–423. doi: 10.1016/j.rse.2004.04.011

Garcia-Lazaro, J. R., Moreno-Ruiz, J. A., Riano, D., and Arbelo, M. (2018). Estimation of Burned Area in the Northeastern Siberian Boreal Forest from a Long-Term Data Record (LTDR) 1982-2015 Time Series. *Remote Sens.* 10:940. doi: 10.3390/rs10060940

Garreaud, R. D., Boisier, J. P., Rondanelli, R., Montecinos, A., Sepúlveda, H. H., and Veloso-Aguila, D. (2020). The central Chile mega drought (2010–2018): A climate dynamics perspective. *Int. J. Climatol.* 40, 421–439. doi: 10.1002/joc.6219

Gibson, R., Danaher, T., Hehir, W., and Collins, L. (2020). A Remote Sensing approach to mapping fire severity in south-eastern Australia using sentinel 2 and random forest. *Remote Sens. Environ.* 240:111702. doi: 10.1016/j.rse.2020.111702

Giglio, L., Boschetti, L., Roy, D. P., Humber, M. L., and Justice, C. O. (2018). The Collection 6 MODIS burned area mapping algorithm and product. *Remote Sens. Environ.* 217, 72–85. doi: 10.1016/j.rse.2018.08.005

Hagolle, O., Huc, M., Pascual, D. V., and Dedieu, G. (2010). A multi-temporal method for cloud detection, applied to FORMOSAT-2, VENμS, LANDSAT and SENTINEL-2 images. *Remote Sens. Environ.* 114, 1747–1755. doi: 10.1016/j.rse.2010.03.002

Hall, J. V., Zibtsev, S. V., Giglio, L., Skakun, S., Myroniuk, V., Zhuravel, O., et al. (2021). Environmental and political implications of underestimated cropland burning in Ukraine. *Environ. Res. Lett.* 16:064019. doi: 10.1088/1748-9326/abfc04

Hansen, M. C., Potapov, P. V., Moore, R., Hancher, M., Turubanova, S. A., Tyukavina, A., et al. (2013). High-resolution global maps of 21st-century forest cover change. *Science* 342, 850–853. doi: 10.1126/science.1244693

Hawbaker, T. J., Vanderhoof, M. K., Beal, Y.-J., Takacs, J. D., Schmidt, G. L., Falgout, J. T., et al. (2017). Mapping burned areas using dense time-series of Landsat data. *Remote Sens. Environ.* 198, 504–522. doi: 10.1016/j.rse.2017.06.027

Hawbaker, T. J., Vanderhoof, M. K., Schmidt, G. L., Beal, Y.-J., Picotte, J. J., Takacs, J. D., et al. (2020). The Landsat Burned Area algorithm and products for the conterminous United States. *Remote Sens. Environ.* 244:111801. doi: 10.1016/j.rse.2020.111801

Huete, A. R. (1988). A soil-adjusted vegetation index (SAVI). *Remote Sens. Environ.* 25, 295–309.

Johnston, F. H., Borchers-Arriagada, N., Morgan, G. G., Jalaludin, B., Palmer, A. J., Williamson, G. J., et al. (2021). Unprecedented health costs of smoke-related PM 2.5 from the 2019–20 Australian megafires. *Nat. Sustainabil.* 4, 42–47. doi: 10.1038/s41893-020-00610-5

Jones, M. W., Smith, A., Betts, R., Canadell, J. G., Prentice, I. C., and Le Quéré, C. (2020). Climate change increases the risk of wildfires. *ScienceBrief Rev.* 116:117.

Key, C., and Benson, N. (2005). "Landscape assessment: Ground measure of severity, the composite burn index; and remote sensing of severity, the normalized burn ratio," in *FIREMON: Fire effects monitoring and inventory system*, (Ogden, UT: USDA Forest Service, Rocky Mountain Research Station).

Khanna, S., Palacios-Orueta, A., Whiting, M. L., Ustin, S. L., Riaño, D., and Litago, J. (2007). Development of angle indexes for soil moisture estimation, dry matter detection and land-cover discrimination. *Remote Sens. Environ.* 109, 154–165. doi: 10.1016/j.rse.2006.12.018

Koutsias, N., and Pleniou, M. (2021). A rule-based semi-automatic method to map burned areas in Mediterranean using Landsat images–revisited and improved. *Int. J. Digit. Earth* 14, 1602–1623. doi: 10.1080/17538947.2021.1962994

Lasaponara, R., and Tucci, B. (2019). Identification of Burned Areas and Severity Using SAR Sentinel-1. *IEEE Geosci. Remote Sens. Lett.* 16, 917–921. doi: 10.1109/LGRS.2018.2888641

Li, Q., Qiu, C., Ma, L., Schmitt, M., and Zhu, X. X. (2020). Mapping the land cover of Africa at 10 m resolution from multi-source Remote Sensing data with Google Earth Engine. *Remote Sens.* 12:602. doi: 10.3390/rs12040602

Lizundia-Loiola, J., Otón, G., Ramo, R., and Chuvieco, E. (2020). A spatio-temporal active-fire clustering approach for global burned area mapping at 250 m from MODIS data. *Remote Sens. Environ.* 236:111493. doi: 10.1016/j.rse.2019.111493

Loboda, T., O'Neal, K., and Csiszar, I. (2007). Regionally adaptable dNBR-based algorithm for burned area mapping from MODIS data. *Remote Sens. Environ.* 109, 429–442. doi: 10.1016/j.rse.2007.01.017

Long, T. F., Zhang, Z. M., He, G. J., Jiao, W. L., Tang, C., Wu, B. F., et al. (2019). 30 m resolution global annual burned area mapping based on landsat images and google earth engine. *Remote Sens.* 11:489. doi: 10.3390/rs11050489

Mallinis, G., and Koutsias, N. (2012). Comparing ten classification methods for burned area mapping in a Mediterranean environment using Landsat TM satellite data. *Int. J. Remote Sens.* 33, 4408–4433. doi: 10.1080/01431161.2011.648284

Martín, M. P., Gómez, I., and Chuvieco, E. (2006). Burnt Area Index (BAIM) for burned area discrimination at regional scale using MODIS data. *For. Ecol. Manage.* 234:S221. doi: 10.1016/j.foreco.2006.08.248

Mutanga, O., Adam, E., and Cho, M. A. (2012). High density biomass estimation for wetland vegetation using WorldView-2 imagery and random forest regression algorithm. *Int. J. Appl. Earth Observ. Geoinform.* 18, 399–406. doi: 10.1016/j.jag.2012.03.012

Nguyen, H. T. T., Doan, T. M., Tomppo, E., and Mcroberts, R. E. (2020). Land Use/land cover mapping using multitemporal Sentinel-2 imagery and four classification methods—A case study from Dak Nong, Vietnam. *Remote Sens.* 12:1367. doi: 10.3390/rs12091367

Noojipady, P., Morton, C. D., Macedo, N. M., Victoria, C. D., Huang, C., Gibbs, K. H., et al. (2017). Forest carbon emissions from cropland expansion in the Brazilian Cerrado biome. *Environ. Res. Lett.* 12:025004. doi: 10.1088/1748-9326/aa5986

Oliva, P., and Chuvieco, E. (2013). Assessment of the discrimination ability of MERIS spectral data for burned area mapping using ROC curves. *GeoFocus Rev. Int. Cienc. Tecnol. Inform. Geográfica* 13, 41–65.

Otsu, N. (1979). A threshold selection method from gray-level histograms. *IEEE Trans. Syst. Man Cybernet.* 9, 62–66. doi: 10.1109/TSMC.1979.4310076

Padilla, M., Stehman, S. V., Ramo, R., Corti, D., Hantson, S., Oliva, P., et al. (2015). Comparing the accuracies of Remote Sensing Global burned area products using stratified random sampling and estimation. *Remote Sens. Environ.*160, 114–121. doi: 10.1016/j.rse.2015.01.005

Palacios-Orueta, A., Khanna, S., Litago, J., Whiting, M. L., and Ustin, S. L. (2006). "Assessment of NDVI and NDWI spectral indices using MODIS time series analysis and development of a new spectral index based on MODIS shortwave infrared bands," in *Proceedings of the 1st international conference of Remote Sensing and geoinformation processing*, Trier.

Ramo, R., and Chuvieco, E. (2017). Developing a random forest algorithm for MODIS global burned area classification. *Remote Sens.* 9:1193. doi: 10.3390/rs9111193

Ramo, R., Garcia, M., Rodriguez, D., and Chuvieco, E. (2018). A data mining approach for global burned area mapping. *Int. J. Appl. Earth Observ. Geoinform.* 73, 39–51. doi: 10.1016/j.jag.2018.05.027

Ramo, R., Roteta, E., Bistinas, I., Van Wees, D., Bastarrika, A., Chuvieco, E., et al. (2021). African burned area and fire carbon emissions are strongly impacted by small fires undetected by coarse resolution satellite data. *Proc. Natl. Acad. Sci. U.S.A.* 118:e2011160118. doi: 10.1073/pnas.2011160118

Randerson, J., Chen, Y., Van Der Werf, G., Rogers, B., and Morton, D. (2012). Global burned area and biomass burning emissions from small fires. *J. Geophys. Res. Biogeosci.* 117:G04012. doi: 10.1029/2012JG002128

Rodriguez-Galiano, V. F., Ghimire, B., Rogan, J., Chica-Olmo, M., and Rigol-Sanchez, J. P. (2012). An assessment of the effectiveness of a random forest classifier for land-cover classification. *ISPRS J. Photogramm. Remote Sens.* 67, 93–104. doi: 10.1016/j.isprsjprs.2011.11.002

Roteta, E., Bastarrika, A., Franquesa, M., and Chuvieco, E. (2021a). Landsat and Sentinel-2 Based Burned Area Mapping Tools in Google Earth Engine. *Remote Sens.* 13:816. doi: 10.3390/rs13040816

Roteta, E., Bastarrika, A., Ibisate, A., and Chuvieco, E. (2021b). A preliminary global automatic burned-area algorithm at medium resolution in google earth engine. *Remote Sens.* 13:4298. doi: 10.3390/rs13214298

Roteta, E., Bastarrika, A., Padilla, M., Storm, T., and Chuvieco, E. (2019). Development of a Sentinel-2 burned area algorithm: Generation of a small fire database for sub-Saharan Africa. *Remote Sens. Environ.* 222, 1–17. doi: 10.1016/j.rse.2018.12.011

Rouse, J. Jr., Haas, R. H., Deering, D., Schell, J., and Harlan, J. C. (1974). *"Monitoring the vernal advancement and retrogradation (green wave effect) of natural vegetation"*. Greenbelt, MD: NASA/GSFC Type III Final Report, 371.

Seydi, S. T., Akhoondzadeh, M., Amani, M., and Mahdavi, S. (2021). Wildfire damage assessment over Australia Using Sentinel-2 Imagery and MODIS land cover product within the google earth engine cloud platform. *Remote Sens.* 13:220. doi: 10.3390/rs13020220

Silveira, E. M., Silva, S. H. G., Acerbi-Junior, F. W., Carvalho, M. C., Carvalho, L. M. T., Scolforo, J. R. S., et al. (2019). Object-based random forest modelling of aboveground forest biomass outperforms a pixel-based approach in a heterogeneous and mountain tropical environment. *Int. J. Appl. Earth Observ. Geoinform.* 78, 175–188. doi: 10.1016/j.jag.2019.02.004

Smiraglia, D., Filipponi, F., Mandrone, S., Tornato, A., and Taramelli, A. (2020). Agreement index for burned area mapping: Integration of multiple spectral indices using Sentinel-2 satellite images. *Remote Sens.* 12:1862. doi: 10.3390/rs12111862

Sulova, A., and Jokar Arsanjani, J. (2020). Exploratory analysis of driving force of wildfires in Australia: An application of machine learning within Google earth engine. *Remote Sens.* 13:10. doi: 10.3390/rs13010010

Tornos, L., Huesca, M., Dominguez, J. A., Moyano, M. C., Cicuendez, V., Recuero, L., et al. (2015). Assessment of MODIS spectral indices for determining rice paddy agricultural practices and hydroperiod. *ISPRS J. Photogramm. Remote Sens.* 101, 110–124. doi: 10.1016/j.isprsjprs.2014.12.006

Trigg, S., and Flasse, S. (2001). An evaluation of different bi-spectral spaces for discriminating burned shrub-savannah. *Int. J. Remote Sens.* 22, 2641–2647. doi: 10.1080/01431160110053185

Tsai, Y. H., Stow, D., Chen, H. L., Lewison, R., An, L., and Shi, L. (2018). Mapping vegetation and land use types in Fanjingshan National Nature Reserve using google earth engine. *Remote Sens.* 10:927. doi: 10.3390/rs10060927

Tsela, P., Wessels, K., Botai, J., Archibald, S., Swanepoel, D., Steenkamp, K., et al. (2014). Validation of the two standard MODIS satellite burned-area products and an empirically-derived merged product in South Africa. *Remote Sens.* 6, 1275–1293. doi: 10.3390/rs6021275

Turco, M., Jerez, S., Augusto, S., Tarín-Carrasco, P., Ratola, N., Jiménez-Guerrero, P., et al. (2019). Climate drivers of the 2017 devastating fires in Portugal. *Sci. Rep.* 9:13886. doi: 10.1038/s41598-019-50281-2

Valencia, G. M., Anaya, J. A., Velásquez, É. A., Ramo, R., and Caro-Lopera, F. J. (2020). About validation-comparison of burned area products. *Remote Sens.* 12:3972. doi: 10.3390/rs12233972

van der Werf, G. R., Randerson, J. T., Giglio, L., Van Leeuwen, T. T., Chen, Y., Rogers, B. M., et al. (2017). Global fire emissions estimates during 1997-2016. *Earth Syst. Sci. Data* 9, 697–720. doi: 10.5194/essd-9-697-2017

Vanderhoof, M. K., Brunner, N., Beal, Y. J. G., and Hawbaker, T. J. (2017). Evaluation of the US geological survey landsat burned area essential climate variable across the conterminous US using commercial high-resolution imagery. *Remote Sens.* 9:743. doi: 10.3390/rs9070743

Veraverbeke, S., Harris, S., and Hook, S. (2011). Evaluating spectral indices for burned area discrimination using MODIS/ASTER (MASTER) airborne simulator data. *Remote Sens. Environ.*115, 2702–2709. doi: 10.1016/j.rse.2011.06.010

Wang, L., Diao, C., Xian, G., Yin, D., Lu, Y., Zou, S., et al. (2020). *A summary of the special issue on Remote Sensing of land change science with Google earth engine*. Amsterdam: Elsevier. doi: 10.1016/j.rse.2020.112002

Yebra, M., Quan, X. W., Riano, D., Larraondo, P. R., Van Dijk, A., and Cary, G. J. (2018). A fuel moisture content and flammability monitoring methodology for continental Australia based on optical Remote Sensing. *Remote Sens. Environ.* 212, 260–272. doi: 10.1016/j.rse.2018.04.053

Zhang, M., Wu, B., and Meng, J. (2014). Quantifying winter wheat residue biomass with a spectral angle index derived from China Environmental Satellite data. *Int. J. Appl. Earth Observ. Geoinform.* 32, 105–113. doi: 10.1016/j.jag.2014.03.020